



Development of integration-type silicon-on-insulator monolithic pixel detectors using a float zone silicon

S. Mitsui^{a,*}, Y. Arai^b, T. Miyoshi^b, A. Takeda^c

^a Venture Business Laboratory, Organization of Frontier Science and Innovation, Kanazawa University, Kakumamachi, Kanazawa, Ishikawa, 920-1192, Japan

^b Institute of Particle and Nuclear Studies, High Energy Accelerator Research Organization (KEK), 1-1 Oho, Tsukuba, Ibaraki, 305-0801, Japan

^c Faculty of Engineering, University of Miyazaki, 1-1 Gakuen kibanadai nishi, Miyazaki, Miyazaki, 889-2192, Japan

ARTICLE INFO

Keywords:

SOI pixel detector
INTPIX4
X-ray imaging
X-ray detector
Float zone silicon
Czochralski silicon

ABSTRACT

In this paper, we describe the development of monolithic pixel detectors using silicon-on-insulator (SOI) technology for a rapid X-ray residual stress measurement system. Conventional two-dimensional X-ray detectors are not suitable for rapid X-ray residual stress measurement because of their large pixel size and slow readout. For this reason, we developed highly sensitive SOI monolithic pixel detectors that are made up of smaller pixels and can provide a more rapid X-ray residual stress measurement readout. The detectors are fabricated using a 0.2 μm CMOS fully-depleted SOI process (Lapis Semiconductor Co., Ltd). The SOI wafer is made by directly bonding a thick, high-resistivity Si wafer and a low-resistivity Si CMOS wafer. The process does not make use of mechanical bump bonding. We developed an integration-type SOI pixel detector, INTPIX4, for a rapid X-ray residual stress measurement system; it uses a float zone (FZ) or Czochralski (Cz) silicon wafer. Cz SOI detectors have been in use since 2005. After 2011, FZ SOI detectors were successfully fabricated. In this paper, we state recent progresses and test results of the SOI monolithic pixel detector using a FZ silicon and compare them with the results obtained using the Cz detector.

1. Introduction

Conventional X-ray detectors are not suitable for X-ray residual stress measurement because of their large pixel size and low-speed read-out. Thus, there is a need for new X-ray detector technology with smaller pixel sizes and high-speed read-outs. To this end, we are developing a rapid residual stress measurement system using an SOI-technology-based two-dimensional X-ray detector.

SOI monolithic pixel detectors have been specifically developed for X-ray and charged particle applications [Ref. [1–8]]. They are made by bonding a thick, high-resistivity sensing wafer to a thin low-resistivity CMOS wafer [Fig. 1]. The SOI detector allows a high circuit density and reduces the amount of materials used due to its monolithic structure. Complex functions can be implemented in a single pixel due to the detector's CMOS technology. The detector does not require a mechanical bump bonding, thus ensuring high yield and low cost. A fully depleted detector has low capacitance at the sense node (approximately 10 fF/pixel), allowing high conversion gain and noise suppression [Ref. [9]]. The SOI technology is based on industry standard technology, thus having a cost benefit and scalability. SOI detectors also have the following additional advantages: no latch-up and prevention of a single event effect. The detectors can run at low power and operate at a wide temperature range from 0.35 to 600

K [Ref. [10,11]]. To prevent the back-gate effect, the buried p-well process is applied to each pixel.

The SOI detectors were fabricated using the 0.2 μm low-leakage fully depleted (FD)-SOI CMOS process of Lapis Semiconductor Co., Ltd. [Ref. [12]]. Table 1 summarizes the main specifications of the SOI processes of float zone (FZ) and Czochralski (Cz) silicon wafers.

SOI pixel detectors and test element groups (TEGs) were fabricated through the multi-project wafer (MPW)-runs organized by KEK, approximately twice a year. A mask of $24.6 \times 30.8 \text{ mm}^2$ is shared to reduce the production cost. Many institutes and universities, from Japan and several other countries, contribute to the MPW run.

2. INTPIX4

We developed the integration-type SOI pixel detector, INTPIX4 for a rapid X-ray residual stress measurement system [Ref. [13]]. Its chip size was $10.3 \times 15.5 \text{ mm}^2$, and its effective area was $8.704 \times 14.144 \text{ mm}^2$. The number of pixels was 512×832 , each of size $17 \times 17 \mu\text{m}^2$ and comprising a correlated double sampling (CDS) circuit to reduce the reset noise [Ref. [14]]. Fig. 2 shows the schematic of the on-pixel circuit. The typical symbols in Fig. 2 is listed in Table 2. The signal in the pixel is read out using the following procedure [Ref. [15]].

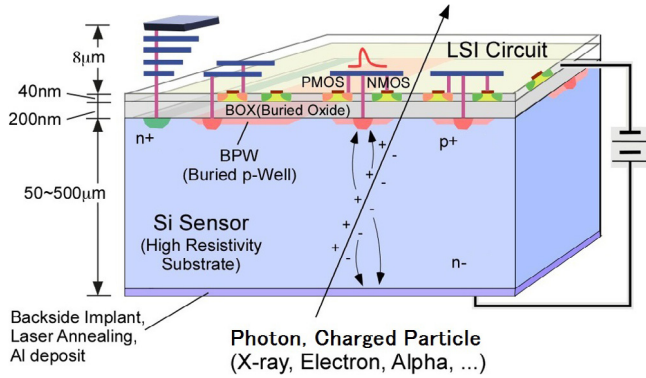
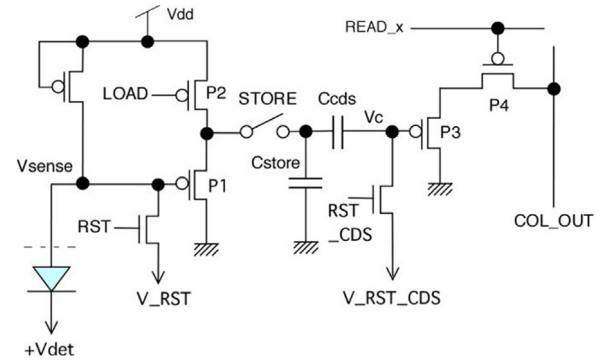
* Corresponding author.

E-mail address: smitsui@staff.kanazawa-u.ac.jp (S. Mitsui).

Table 1

Main specifications of the SOI processes of FZ and Cz silicon wafers.

Process	0.2 μm low-leakage fully depleted (FD)-SOI CMOS 1 Poly, 5 Metal layers (MIM Capacitor and DMOS option) Core I/O voltage: 1.8 (3.3) V
SOI wafer (8-in.)	Top Si: Cz, $\sim 18 \Omega\text{-cm}$, p-type, $\sim 40 \text{ nm}$ thick Buried Oxide: 200 nm thick Handle wafer thickness: 725 μm -> thinned up to $\sim 300 \mu\text{m}$ in Lapis' processes -> thinned up to $\sim 50 \mu\text{m}$ in commercial processes Handle wafer: Cz (n-type) $\sim 700 \Omega\text{-cm}$, FZ (n-type) $> 7 \text{ k}\Omega\text{-cm}$
Back-side process	Mechanical grind -> Chemical etching -> Back-side implant -> Laser annealing -> Al plating

**Fig. 1.** Structure of the SOI pixel detector.**Fig. 2.** Schematic of the on-pixel circuit for INTPIX4, which has a CDS function and 2 capacitors: Cstore and Ccds [Ref. [13]].**Table 2**

Meaning of typical symbols in Fig. 2.

Ccds	The capacitor for CDS.
Cstore	The capacitor to store the input signal.
RST	The reset switch to set the sense node to V_RST.
RST_CDS	The reset switch to set the Vc to V_RST_CDS.
STORE	The switch to store the input signal from the sense node.

- (1) At first, RST, RST_CDS, and STORE switches are closed.
- (2) Before starting the exposure, the Vc is set to the voltage of V_RST_CDS, and the sense node, Vsense is set to the voltage of V_RST.
- (3) The RST switch is opened before opening the RST_CDS switch so as not to read out the reset noise from the RST switch.
- (4) The exposure starts after opening the RST_CDS switch.
- (5) The input signal is amplified by the source follower circuit, P1. The potential Vc follows the potential of the amplified input voltage during exposure.
- (6) The starting value of Vc is V_RST_CDS.
- (7) Vc is read out when the READ_x switch is closed.

INTPIX4 consists of 13 segments, each of which consist of 512×64 pixels [Fig. 3]. The signals of all pixels are read out from one terminal using 6- and 4-bit column address decoders and a 9-bit row address decoder [Fig. 4]. Alternatively, the signals are read out in 13 parallels using only the 6-bit column address decoder. These analog signals are converted to digital signals by analog-to-digital converters on a readout board.

The resistivity and thickness of the n-type handle wafer are respectively over $700 \Omega\text{-cm}$ and $260 \mu\text{m}$ for Cz, and over $7 \text{ k}\Omega\text{-cm}$ and $500 \mu\text{m}$ for FZ. Both front- and back-side illuminations are available.

3. Readout board

Fig. 5 shows a general-purpose evaluation board for SOI pixel detectors. It comprises an SOI evaluation board with SiTCP 2 (SEABAS2) and a sub board for INTPIX4. The SEABAS2 has a Gigabit Ethernet

converter for data transfer connected to a data acquisition PC. The user field-programmable gate array (FPGA) vertex5 and the FPGA for SiTCP [Ref. [16]] are mounted on the board. The operation clock frequency is 50 MHz with an operational voltage of $+3.3 \text{ V}$, and -3.3 V for nuclear instrument module (NIM) signals. We implemented a 12-bit 16ch ADC, a 4ch DAC, and an NIM I/O interface. Due to the use of a Gigabit Ethernet converter, the SEABAS2 can read rapidly, operating at approximately 90 fps with an INTPIX4 chip. Thus, even an X-ray movie can be captured. It is sufficient for rapid X-ray residual stress measurement.

Fig. 6 shows the X-ray image of a medical stent wire; this was shot using a 33.3 keV monochromatic X-ray at a photon factory in KEK. Its integration time is $200 \mu\text{s}$; 250 frames are captured, thus making the total integration time 50 ms. The stent wire is $40 \mu\text{m}$ in diameter and made of nickel titanium. The amount of acrylic case is consistent with the human body. The stent wire is clearly seen by using INTPIX4 and SEABAS2.

4. Performance of FZ and Cz SOI detectors

4.1. Leakage current improvement

Leakage current directly affects the quality of X-ray images and integration time. Therefore, it is important to measure leakage current. Cz SOI detectors have been used since 2005. FZ SOI detectors were first successfully fabricated and used in 2011, which decreased the leakage current [Fig. 7]. In this paper, the performance of FZ INTPIX4 detectors is principally reported, along with the comparison of FZ and Cz SOI detectors.

4.2. Spatial resolution

X-ray residual stress measurement requires high spatial resolution for precision measurement of diffracted X-rays. We evaluated the spatial resolution through direct radiography. The X-ray was directed to illuminate the FZ detector from the back-side using a test chart

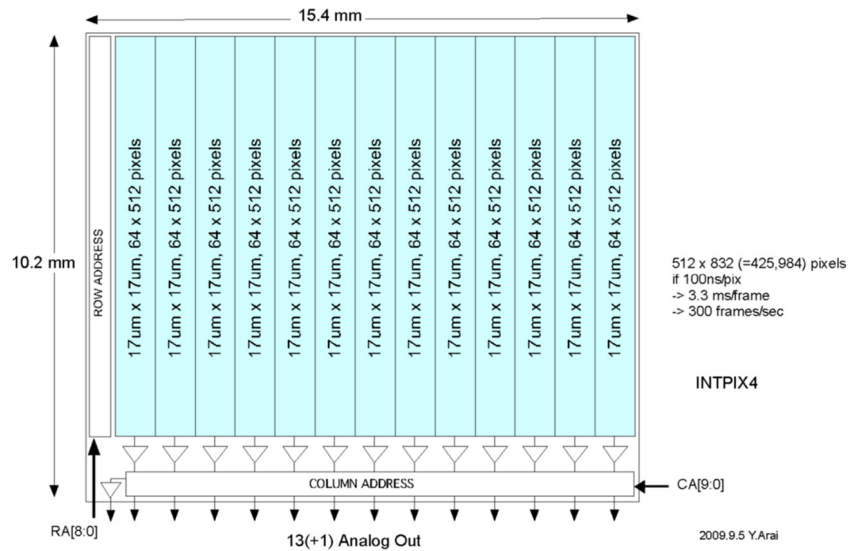


Fig. 3. Block diagram of INTPIX4 [Ref. [13]].

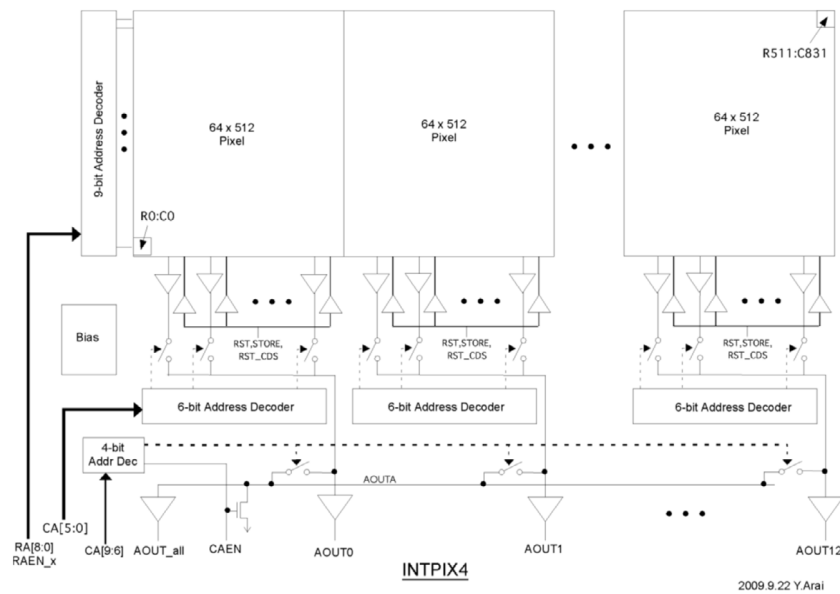


Fig. 4. Detailed block diagram of I/O Path in INTPIX4 [Ref. [13]].

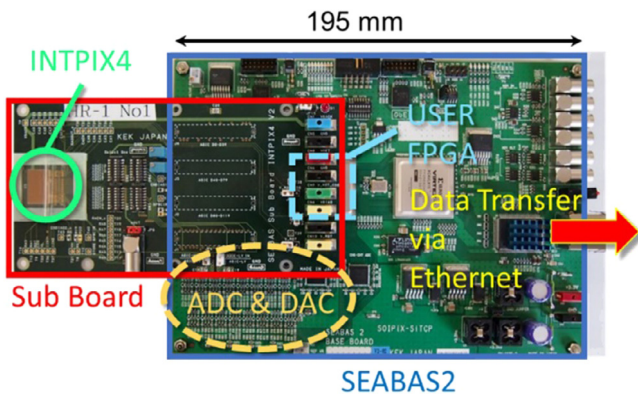


Fig. 5. SEABAS2 and INTPIX4 sub board.

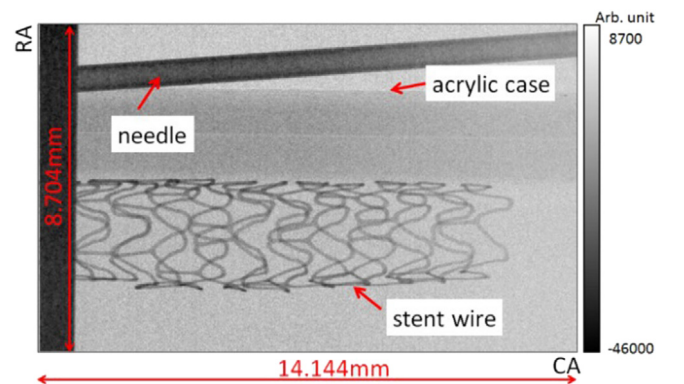


Fig. 6. X-ray image of medical stent wire.

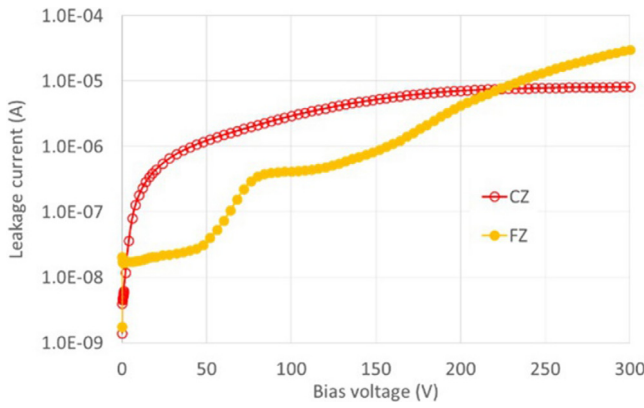


Fig. 7. Comparison of leakage current in FZ and Cz detectors.

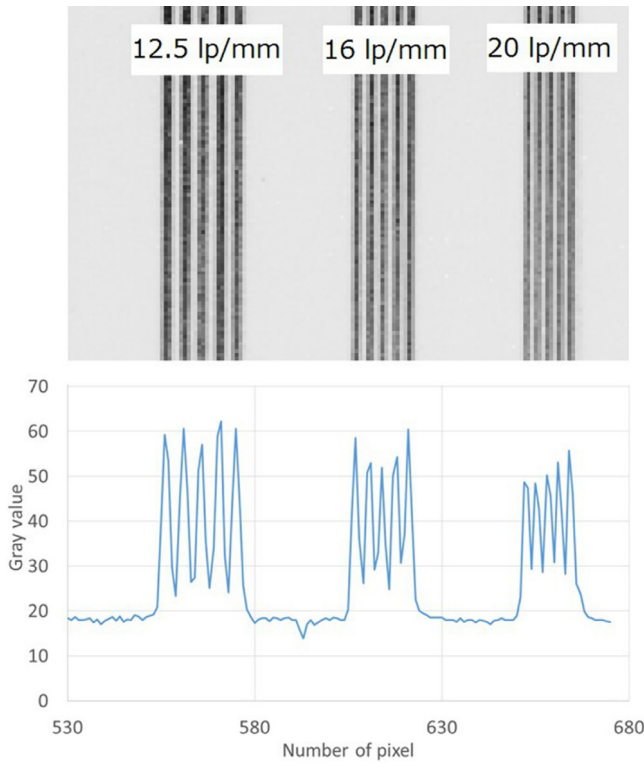


Fig. 8. A negative photograph of the test chart (above), Gray values of 12.5, 16, and 20 lp/mm (below).

with 12.5, 16, and 20 lp/mm (line pairs per mm) slits, with window widths of 40, 31.25, and 25 μm , respectively. Fig. 8 shows a negative photograph of the X-ray image of the FZ detector and its gray values. The power of the X-ray generator was 30 kV, 20 mA, in which a Mo target was installed, and a characteristic X-ray of 17.48 keV was generated. In addition, the applied bias voltage of the FZ detector was 100 V, with 250 μs integration time; we integrated 1000 frames.

The contrast transfer function (CTF) is defined as

$$\text{CTF}(\%) = \frac{I_{\text{MAX}} - I_{\text{GAP}}}{I_{\text{MAX}} - I_{\text{MIN}}}, \quad (1)$$

where I_{MAX} is the average of gray values at slits, I_{GAP} is the average of gray values between slits, and I_{MIN} is the average of gray values of the base line not irradiated by X-rays. Fig. 9 shows the CTF of the 500 μm thick FZ detector and 260 μm thick Cz detector [Ref. [17]]. The CTFs of FZ and Cz were respectively 66% and 78% at 20 lp/mm. The CTF of FZ was slightly poorer than that of Cz because of its thickness. The

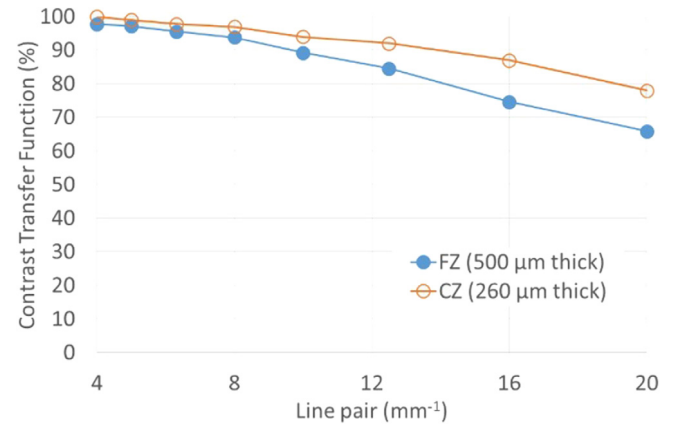
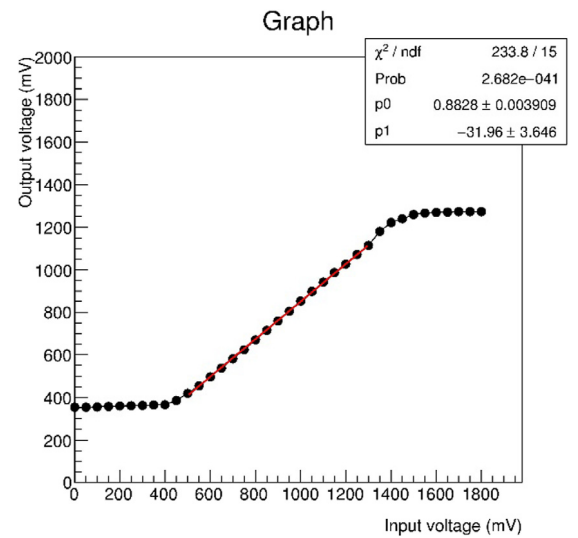
Fig. 9. CTF of the FZ detector of 500 μm thickness and the Cz detector of 260 μm thickness.

Fig. 10. Dependence of the analog output voltage on the input CDS reset voltage.

generated electron-hole pairs spread while drifting from the back-side through a thicker Si bulk. For X-ray residual stress measurement, these spatial resolutions of FZ and Cz are sufficient to detect the diffracted X-ray.

4.3. Circuit gain

Evaluation of circuit gain is essential for correcting the uniformity of the pixel's analog output. For this reason, we evaluated the circuit gain of FZ INTPIX4. The circuit gain in a pixel was measured using the coefficient of proportionality of the analog voltage output to the input CDS reset voltage, $V_{\text{RST_CDS}}$. The analog output is proportional to the input CDS reset voltage over the threshold voltage, up to the saturation voltage [Fig. 10]. Furthermore, the circuit gain was obtained through the slope of the proportional region. Fig. 11 shows the circuit gain of all pixels. Moreover, the FZ detector resulted in a circuit gain of 0.87 ± 0.02 , which is consistent with the circuit gain of Cz, that is, 0.823 ± 0.001 [Ref. [16]].

4.4. Energy spectrum

To evaluate the output characteristics depending on the X-ray energy, the energy spectrum of the X-ray was measured. We obtained the energy spectrum of the characteristic X-rays of Mo and Cu targets

Gain map of INTPIX4

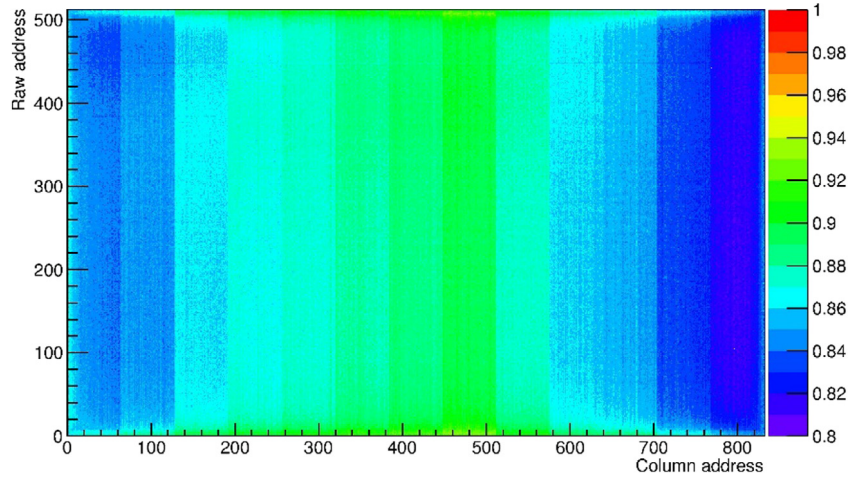


Fig. 11. Linearity of circuit gain of FZ INTPIX4.

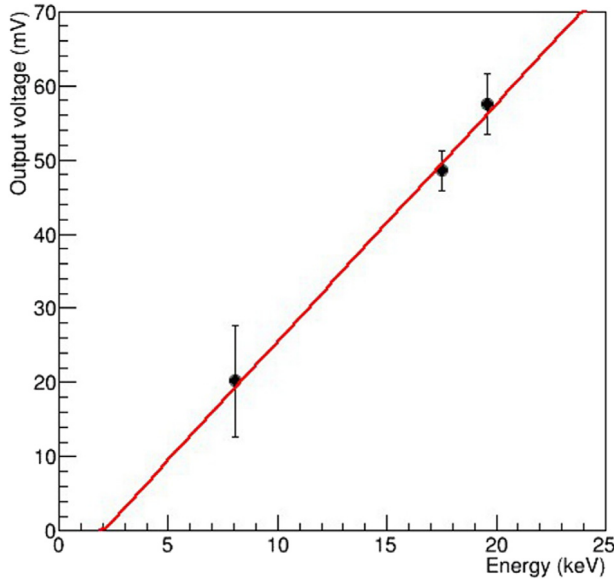


Fig. 12. Detector gain of FZ SOI detector.

by using the X-ray generator. The X-rays were irradiated towards the back-side of the detector, and the spectrum was captured at room temperature (approximately 25 °C). The bias voltage was 200 V. The power of the X-ray tube with a Mo target was 30 kV, 20 mA, and with Cu target it was 20 kV, 20 mA. The collected charge was evaluated by clustering several pixels because the electron-hole pairs generated through X-rays spread in the Si bulk. The collected charges of the Mo and Cu targets were evaluated by clustering 9 and 25 pixels, respectively. The energies of the characteristic X-rays of Mo- K_α , Mo- K_β , and Cu- K_α were 17.48, 19.61, and 8.05 keV, respectively. The resulting detector gain was 13.1 $\mu\text{V}/\text{e}$, which was calculated using the output voltage slope at each energy [Fig. 12]. The full-width half-maximum (FWHM) of 624 electrons was obtained as 12.8% at 17.48 keV. The detector gain and FWHM of the Cz detector were 12.61 $\mu\text{V}/\text{e}$, and 13.4% at 13.95 keV [Ref. [16]]. The detector gain and FWHM of both FZ and Cz were consistent.

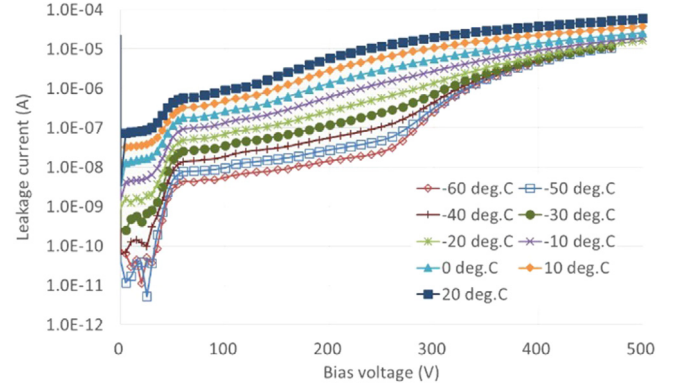


Fig. 13. I-V characteristics of FZ detector from -60 °C to +20 °C up to 500 V bias voltage.

4.5. I-V characteristics

I-V characteristics are the simplest indicators to evaluate the quality of the detectors. To analyze the leakage current component, we investigated the I-V characteristics at temperatures from -60 °C to +20 °C at 10 °C steps. At each temperature, there was no breakdown up to 500 V for the FZ detector [Fig. 13]. The leakage current increase at approximately 280 V was probably caused by the depletion region reaching the back surface. The reason for the increase of approximately 50 V is still under investigation. The activation energy can be obtained through the Arrhenius plot as follows:

$$I = Ae^{\frac{-E_a}{kT}}, \quad (2)$$

where I is a leakage current, A is a coefficient, E_a is activation energy, k is the Boltzmann constant, and T is the absolute temperature. After plotting the current value at each temperature and fitting the plots with the Arrhenius equation, the activation energy was obtained as the slope of the curves [Fig. 14], and it was 0.55 eV at 30 V. It was consistent with that of the Cz detector: 0.56 eV [Ref. [16]]. The activation energy of the FZ detector was evaluated at 30 V because of the increase in the leakage current over 50 V. Moreover, the leakage current at the low temperature region was avoided in the calculation because it exceeded the measurement limit of the ammeter. The results showed that the recombination current in the depletion zone was dominant, because the activation energy is half of the bandgap energy of silicon.

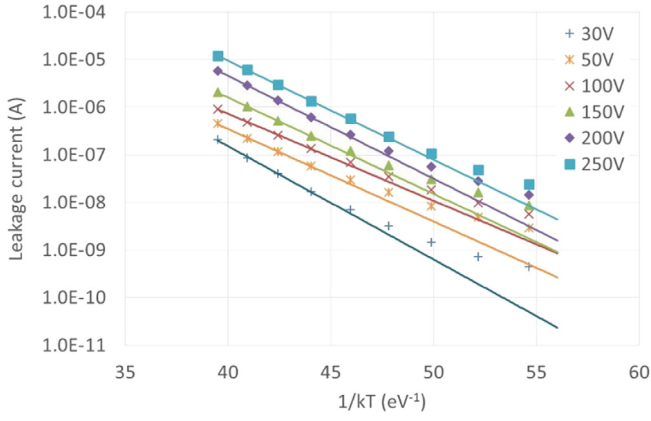
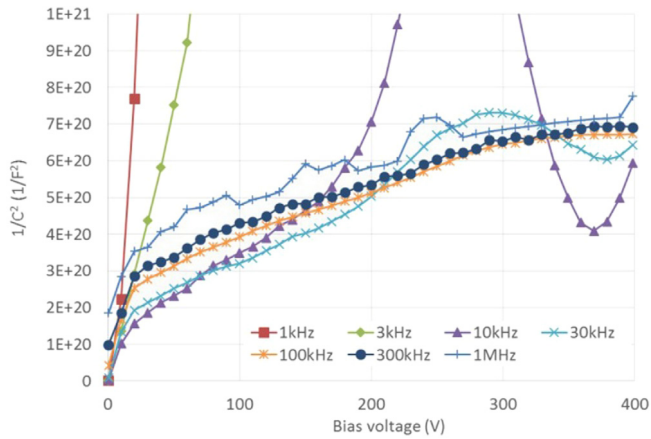


Fig. 14. Arrhenius plots from 30 to 250 V bias voltage.

Fig. 15. Bias voltage dependence of $1/(\text{the body capacitance})^2$ with the FZ detector from 1 kHz to 1 MHz measurement frequency.

4.6. C–V characteristics

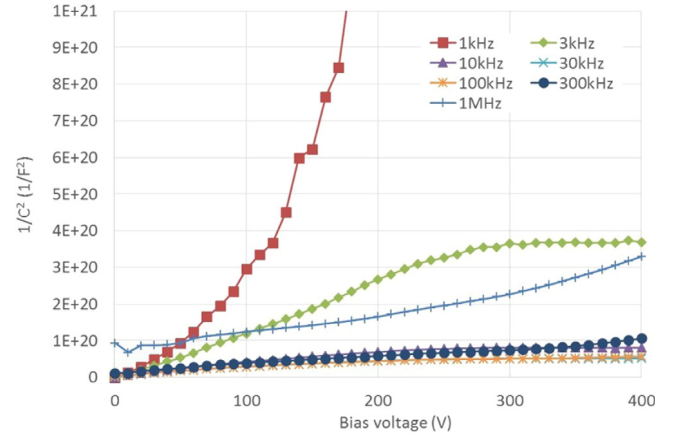
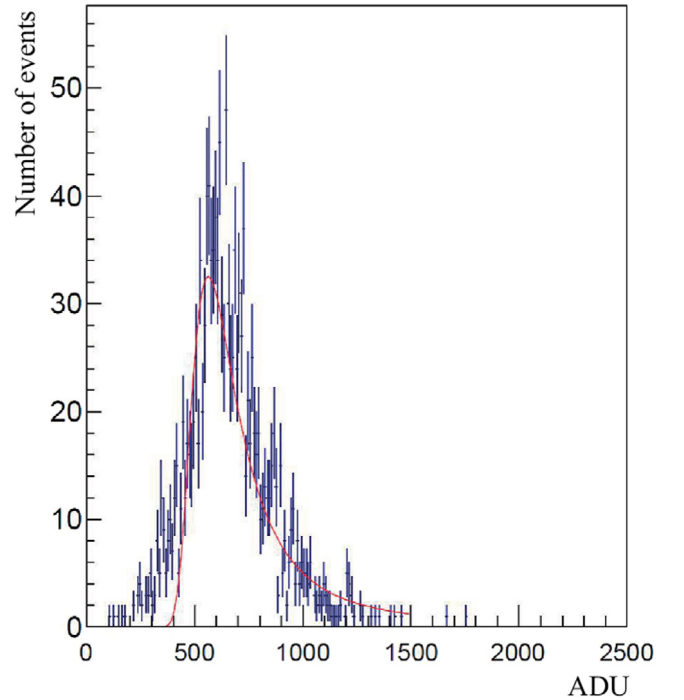
The full depletion voltage, which is needed to determine the operation voltage, was obtained by analyzing the C–V characteristics. We measured the body capacitance of FZ and Cz detectors while applying the voltage. The body capacitance was measured using an LCR meter by applying a bias voltage of up to 400 V at room temperature. The inverse square of the body capacitance is proportional to the bias voltage until the detector reaches full depletion.

$$\frac{1}{C_{\text{bulk}}^2} = \frac{2}{S^2 q \epsilon} \frac{N_A + N_D}{N_A N_D} V, \quad (3)$$

where C_{bulk} is the body capacitance of the detector, S is the depleted area, q is the elementary charge, ϵ is the permittivity of silicon, N_A is the acceptor density of the sense node, N_D is the bulk donor density, and V is the applied voltage. After full depletion, the body capacitance becomes constant. The capacitance was measured at the standard measurement frequencies of the LCR meter from 1 kHz to 1 MHz [Figs. 15 and 16]. The full depletion voltages of FZ were evaluated as 321 V at 100 kHz, and 325 V at 300 kHz. Furthermore, those of Cz were evaluated as 238 V at 30 kHz, and 239 V at 10 kHz.

4.7. Beta-ray source test

We performed beta-ray source tests of ^{90}Sr to evaluate the performance of INTPIX4 for charged particle detection. The beta rays from the

Fig. 16. Bias voltage dependence of $1/(\text{the body capacitance})^2$ with the Cz detector from 1 kHz to 1 MHz measurement frequency.Fig. 17. Energy distribution of beta rays of ^{90}Sr using the FZ detector.

^{90}Sr source included 2.28 MeV beta rays of ^{90}Y , which can be assumed to be minimum ionization particles (MIPs). The collimator had a hole diameter of 3 mm. The Al attenuator was set on the collimator to reduce low-energy beta rays. The trigger scintillator had dimensions of $10 \times 10 \times 10 \text{ mm}^3$. Moreover, the thicknesses of FZ and Cz detectors were 500 and 260 μm , respectively, with corresponding applied bias voltages of 200 and 100 V, and integration times of 1000 and 400 μs . Figs. 17 and 18 show the energy distribution of FZ and Cz detectors, for which the analog digital units of the signal peaks were 374 and 235, pedestal sigma were approximately 5 and 13, and the signal-to-noise ratios were approximately 75 and 18, respectively. These results show that MIPs are observable by using the SOI detector.

5. Summary

We conclude that the integration-type SOI pixel detector INTPIX4 is suitable for rapid X-ray residual stress measurement. It can capture

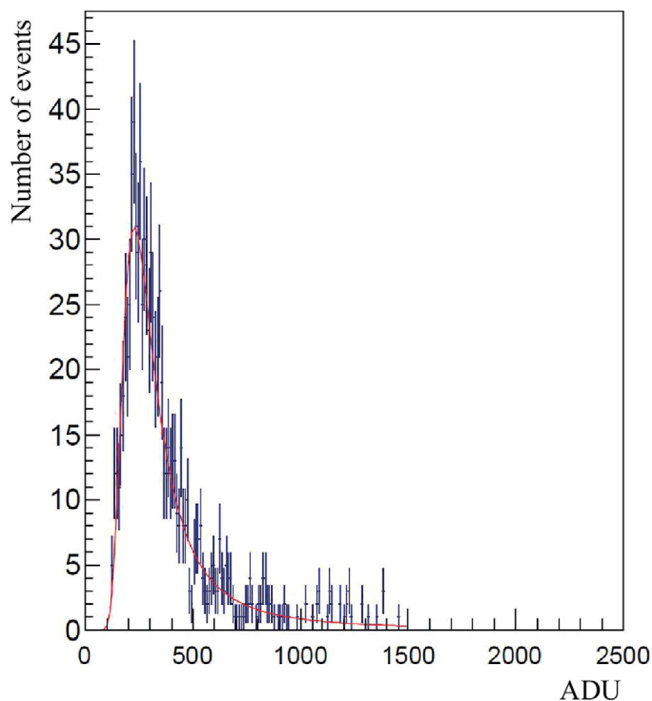


Fig. 18. Energy distribution of beta rays of ^{90}Sr using the Cz detector.

X-ray images with high spatial resolution, high contrast, and high speed. In addition, FZ detectors show good performance similar to that of Cz detectors. The leakage current in FZ detectors is less than that in Cz detectors. However, the fully depleted voltages of FZ detectors are higher than of Cz detectors because of their thicker bulk. In addition, the higher resistivity of FZ detectors (approximately 10 times higher than that of CZ detectors) enables thicker sensing volume at a moderate bias voltage. Further, the amplifier gain, the detector gain, activation energy, and energy resolution of FZ detectors are consistent with those of Cz detectors.

Declaration of competing interest

The authors declare that they have no known competing financial interests or personal relationships that could have appeared to influence the work reported in this paper.

CRediT authorship contribution statement

S. Mitsui: Conceptualization, Methodology, Software, Investigation, Data curation, Writing - original draft, Writing - review & editing, Visualization. **Y. Arai:** Formal analysis, Supervision, Project administration. **T. Miyoshi:** Methodology, Validation. **A. Takeda:** Methodology, Validation.

Acknowledgment

This research was supported by the Program of Development of Advanced Measurement and Analysis Systems from Japan Science and Technology Agency.

References

- [1] T. Miyoshi, et al., Nucl. Instrum. Methods A 824 (2016) 439–442.
- [2] R. Nishimura, Nucl. Instrum. Methods A 831 (2016) 49–54.
- [3] T. Miyoshi, et al., Nucl. Instrum. Methods A 732 (2013) 530–534.
- [4] T. Miyoshi, et al., Procedia 37 (2012) 1039–1045.
- [5] Y. Arai, et al., Nucl. Instrum. Methods A 636 (2011) 31–36.
- [6] Y. Arai, et al., Nucl. Instrum. Methods A 623 (2010) 186–188.
- [7] T. Miyoshi, et al., Nucl. Instrum. Methods A 636 (2011) 237–241.
- [8] T. Miyoshi, et al., in: Proc. IEEE Nuclear Sci. Symp. Conf. Rec. 2010, pp. 1885–1888.
- [9] A. Takeda, et al., JINST 10 (2015) C06005.
- [10] Y. Arai, I. Kurachi, Radiation Imaging Detectors using SOI Technology, Morgan & Claypool Publishers, 2017.
- [11] S.H. Kim, et al., in: Proc. Int. Conf. Technol. Instr. Particle Phys. (TIPP2017), SPPHY 213, 2018, pp. 242–248.
- [12] Lapis Semiconductor Co. Ltd. <<http://www.lapis-semi.com>>.
- [13] Y. Arai, INTPIX4 User's manual, Rev. 0.33 (in Japanese), 2013.
- [14] S.G. Ryu, et al., IEEE Trans. Nucl. Sci. 58 (5) (2011) 2528–2536.
- [15] R. Nishimura, Development and Evaluation of X-Ray Imaging System using SOI Pixel Detector (Doctoral Thesis), SOKENDAI, 2018, (in Japanese).
- [16] T. Uchida, IEEE Trans. Nucl. Sci. 55 (3) (2008) 1631–1637.
- [17] A. Takeda, Test of Integration Type Pixel Detector, SOI Collaboration Meeting, Lawrence Berkeley National Laboratory, 2012, pp. 14–16, <https://kds.kek.jp/indico/event/8865/>.